Yield envelope assessment as a preliminary screening tool to determine carbon capture and storage viability in depleted southern north-sea hydrocarbon reservoirs

Re-submitted to International Journal of Rock Mechanics and Mining Sciences on 28/11/2017

Marcus R. Dobbs,
Robert J. Cuss,
Audrey Ougier-Simonin,
Daniel Parkes,
Caroline C. Graham
British Geological Survey, Keyworth, Nottingham, NG12 5GG, UK
Corresponding author: M.R. Dobbs, British Geological Survey, Keyworth, Nottingham, NG12 5GG, UK. (marc1@bgs.ac.uk)

Key points:

- Yield envelope defined for Sherwood Sandstone Group;
- Stress analysis shows that Sherwood Sandstone Group is a competent reservoir rock and by analogy depletion and injection of CO_2 in parts of the Bunter Sandstone Formation is unlikely to result in deformation of the reservoir rock.
- Acquisition of hydro-mechanical data from onshore analogues of offshore depleted hydrocarbon reservoirs is a cost effective, early assessment screening tool of geomechanical performance of CCS viability.

Abstract: *The use of depleted hydrocarbon reservoirs to store super-critical carbon dioxide is likely to challenge the performance of the storage facility. An early assessment of geomechanical performance during depletion and reinjection can be used as a screening tool to identify viable candidate reservoirs prior to investment in more costly examination. This paper describes a laboratory study of the hydro-mechanical properties of samples from the Sherwood Sandstone Group (SSG), an onshore analogue of the finer grained, lower porosity portions that make up the Bunter Sandstone Formation (BSF). The study provides a yield envelope for this sandstone and demonstrates that it is a competent sandstone at relevant reservoir depths. A theoretical yield envelope has been calculated based on the anticipated in situ stress induced by depletion and reinjection, showing that only the high porosity (35 %), large grain diameter (290 µm) end-member of the BSF is likely to result in deformation of the reservoir rock. Stress analysis of four fields within the Southern North Sea suggest that depletion of 10 MPa will not result in permanent deformation of the reservoirs assuming similar porosity and grainsize characteristics to the SSG tested. Furthermore, re-inflation is unlikely to result in permanent deformation should the injection pressure not exceed the initial pre-production reservoir pore pressure.*

Keywords

Bunter Sandstone Formation; Sherwood Sandstone Group; mechanical properties; permeability; yield; reservoir performance; Hoek-Brown; Mohr-Coulomb.

1 Introduction

The capture of carbon dioxide (CO_2) from large point source emitters and storage in the form of a super-critical fluid within geological formations is a key technology in tackling anthropogenic climate change (1,2). To achieve a reduction in emissions, significant quantities of CO_2 need to be injected into suitable geological formations capable of containing the fluid for thousands of years. It has been estimated that approximately 3.2 billion tonnes (Gt) of CO_2 need to be injected annually (3). Depleted hydrocarbon reservoirs represent a significant national resource within the UK with the potential for storing gigatonnes of CO_2 and aiding UK emission reduction targets. In 2012, the then Department of Energy and Climate Change (DECC) stated that depleted gas fields represent “the most important storage type for the UK”, and “provide a significant proportion of potential future capacity for the nation” (4). Estimates suggest up to 9.9 Gt of UK storage capacity comes from reservoirs that have previously contained hydrocarbons extracted by the oil and gas industry (5). This form of storage site has a number of benefits, including the generally well-characterised geology and the potential for reutilisation of pre-existing infrastructure for injection activities. They also offer security of storage with an effective top-seal that previously acted as a seal to hydrocarbons, provided no deformation occurred during hydrocarbon extraction. Several demonstration projects have been conducted injecting megatonne scale CO_2 into depleted hydrocarbon reservoirs, including in the Norwegian North Sea at Sleipner (6).

The use of a depleted reservoir will play a role in the performance of the storage facility. The process of hydrocarbon extraction, or depletion, can significantly affect both the reservoir involved and the surrounding rocks. During depletion, reservoir pore pressure will have lowered as hydrocarbon extraction occurred and as a result, the reservoir may have subsided. These activities, therefore, have the potential to cause deformation, movement on faults and/or damage to infrastructure, for example induced seismicity at Groningen (Netherlands; 7) and faulting at Ekofisk (North Sea; 8).

The injection of super-critical fluid into a depleted reservoir will result in an increase in pore pressure, possibly resulting in heave and consequently has the potential to cause additional deformation, movement on faults and/or damage to infrastructure. The use of injection and extraction boreholes can minimise this effect, with water injected at a rate similar to the hydrocarbon extraction rate during drawdown, and extraction of aquifer water at a similar rate to CO_2 injection. Perturbations of reservoir pore-fluid pressures occur when flow out of, or into the reservoir is initiated. These changes in pore pressure, and as a result the stress state, may lead to undesired geomechanical deformation that could affect the integrity of the reservoir and the overlying seal. The long-term impacts of such pore pressure changes, particularly when the reservoir is re-inflated during injection of CO_2, are not well understood and there is a lack of physical data for specific rock types and scenarios. Zoback & Gorelick (3) identified the risk to security from a geomechanical point of view, while Economides & Ehlig-Economides (9) showed that an upper pressure limit exists for carbon capture and storage (CCS), above which the seal is potentially compromised due to the formation of fractures. Verdon *et al.* (10) examined the deformation observed at pilot injection sites and noted that the geomechanical response was: complicated and non-intuitive at Weyburn (Saskatchewan Province, Canada; e.g. 11); small at Sleipner due to the high permeability and large lateral extent of the reservoir (12); and that uplift and microseimic activity was noted at In Salah (Algeria; e.g. 13). Therefore, reservoirs are evaluated on an individual basis, both in terms of their geometry and the properties of the geology present.

The UK's primary offshore oil and gas fields are located within the basins of the East Irish Sea, the Southern North Sea (SNS) and the Northern and Central North Sea (5; 14). Within the SNS basin, CO_2 storage potential has been estimated to be ~17 Gt (14; 15), though a broad range in theoretical capacity is generally reported for saline aquifers. However, oil and gas fields within the area may potentially provide an effective capacity of around 3.9 Gt of CO_2. The annual output of CO_2 in the UK has been calculated as 404 Mt for 2015 (16), of which 136 Mt can be attributed to energy supply and could theoretically be subject to carbon capture and storage. Additional output of CO_2 from other industrial sources could additionally be captured and stored.

Geomechanical data for the Southern North Sea is not readily available, consequently it is difficult to make a reasonable early assessment of reservoir-specific geomechanical performance. Offshore drilling for new borehole core for testing is prohibitively expensive, particularly at such an early stage of CCS development. Consequently, testing of existing borehole core is the most economical way to obtain geomechanical parameters for early reservoir viability assessment.

This paper describes a laboratory study of the mechanical and hydromechanical properties of reservoir sandstone relevant to the Southern North Sea (SNS) basin; sandstone of the Sherwood Sandstone Group (SSG) is the onshore equivalent of the Bunter Sandstone Formation (BSF) from the SNS. Testing included: porosity and density determination by the saturation and buoyancy technique; uniaxial strength and deformability; triaxial strength and deformability; sonic velocity measurements during hydrostatic compression; and transient permeability measurements during hydrostatic compression. Mohr-Coulomb, Hoek-Brown and yield envelope parameters were calculated from the results.

2 Test material and experimental protocols

2.1 Bunter Sandstone Formation and Sherwood Sandstone Group

Given its importance as a storage reservoir both in saline aquifers and depleted fields within the SNS, as well as within the East Irish Sea Basin, the Bunter Sandstone Formation (BSF) was selected as a suitable lithology for the experimental test programme. Parkes *et al.* (17) details the selection of candidate geologies for the current study.

The BSF is Triassic in age and is the upper part of the wider Bacton Group. Onshore in the UK the stratigraphic equivalent is the Sherwood Sandstone Group (SSG). In the North Sea Dutch Sector and the Netherlands the equivalent formation is the Main Bundsandstein Formation of the Lower Germanic Trias Group. Figure 1 shows the stratigraphic correlation of the Triassic succession from the onshore UK across the UK and Netherland sectors of the Southern North Sea.

In the SNS the BSF is red, orange and occasionally white sandstone. It is predominately formed of an upward-coarsening sheet-sand complex, composed of mostly fine-grained sand, but with local areas of coarser-grained sands and conglomerates. The unit varies in thickness across the SNS with a maximum thickness of 600 m in the main depocentre of the Sole Pit Trough (18), although more conservative estimates of 0 – 350 m (average 200 m; 19), 174 – 274 m (average 225m; 20) and over 350 m (21) have been presented. Toward its northern margin the thickness gradually reduces to zero because of erosion under the Hardegsen Disconformity (22). Typically the top of the BSF lies between 1,000 and 1,300 m but is variable due to salt movements (22). The Bunter thins over highs such as the Cleaver Bank High, due to higher erosional rates and greater distance from the original source region. The source of sediment was likely to have been the London-Brabant Massif to the south or the Pennine Massif to the west. BSF was deposited in a range of basin environments during hot, arid, semi-arid climatic conditions. Marginal basin deposits represent a series of coalescing alluvial fans with braided fluvial channels formed during sheet flood events, with interbedded silt layers deposited in lower energy ephemeral lakes (21, 19). Central basin deposits have fewer conglomerates and are interpreted as large, flat plain sheet flood deposits (19).

Generally, the SSG and BSF are composed of well-sorted, round/sub-rounded grains of quartz, feldspar and lithic fragments, with cements of calcite and other carbonates, anhydrite and quartz, as well as feldspar overgrowths, more common near the basin margins. Central basin areas have common halite cement, which can greatly reduce porosities (23). Detrital mineralogy and grain size are not constant in the sandstones across the UK, with variability caused by the distance of the depositional environment from the original source region.

Triassic sandstones in proximal areas like south and south-western England have more abundant feldspar and rock fragments and are referred to as lithic arkoses to sub-arkosic litharenites. Some samples can have up to 30 % feldspar (almost all K-spar), while the more lithic samples can have up to 50 % lithic clasts including, sedimentary, igneous and metamorphic grains. Other than lithic grains and feldspars, simple and polycrystalline quartz account for a high percentage of the remaining constituents, along with minor mica, heavy minerals and opaques (24).

In more distal regions, such as the SNS and outcrops to the north and east of Nottingham, SSG rocks are more fine-grained and are made up of sub arkoses, sub-litharenites and quartz arenites. In the sandstones, total quartz accounts for 50 – 65 % of the whole rock, dominated by simple quartz, with lower amounts of polycrystalline quartz. Other constituents include feldspar (mostly K-spar) (5-10%), rock fragments (10-15%), minor mica, heavy minerals and opaques. Both the feldspar and rock fragments are much rarer than in the proximal sandstones (24).

Parkes *et al.* (17) summarises the diagenetic alteration in the North Sea BSF. The general lithologies of the sandstones are quartz arenites, subfeldspathic arenites and sublithic arenites, composed of detrital quartz (major) and feldspar (minor - mostly K-spar, lesser albite and some perthite) and lithics (cherts, siltstones, mudstones, uncommon quartz-feldspathic rocks, rare volcanics). The sandstones are mostly angular to sub-angular grains with rare well-rounded grains restricted to coarser beds, except for at the top of Lower Volpriehausen and base and middle of Volpriehausen Clay-Siltstone in central part of Southern North Sea basin where well rounded, fine to coarse sands are interpreted as aeolian sands. The primary porosity and mineralogy has been heavily altered in parts of the North Sea. Porosity has been reduced in some areas through compaction and cementation and enhanced in others through cement and detrital framework grain-dissolution.

2.2 Test samples

Potential core material was identified within the British Geological Survey (BGS) Offshore and Onshore collections at Keyworth, UK. Extensive slabbing of core material meant that test samples of sufficient dimensions could not be produced, so no suitable material was identified within the BSF. Therefore, a suitable alternative had to be selected from the onshore equivalent, the Sherwood Sandstone Group (SSG). Potential rocks were assessed to determine their suitability based on the following criteria: 1) a reasonable degree of homogeneity within the selected sample interval to reduce inter-sample heterogeneity; 2) sufficient material to provide the required sample number and dimensions for testing; 3) acceptable proximity to the Southern North Sea fields of interest; and 4) petrophysical properties that fall within the expected range for the Bunter Sandstone Formation in known depleted gas reservoirs.

The material identified as most suitable following the screening process was from Sherwood Sandstone Group from the Staithes No.20 Borehole (NZ71NE/14; E476024 N0517997; Figure 2). This 1.2 km deep borehole was drilled by Cleveland Potash Ltd and is located at the coast within the North Yorkshire Moors National Park, just south of Middlesbrough. At this location the SSG is present between 650 m and 925 m below ground level. The Staithes No.20 Borehole has provided a complete cored sequence through the Triassic strata (Penarth Group), Mercia Mudstone Group and Sherwood Sandstone Group in north Yorkshire. Lithological description for the Staithes No.20 borehole is given for twenty-two samples in Table 1 to show the full range of variation within the SSG at this location.

Thirty-nine samples were selected between 650 m and 870 m depth for preliminary porosity and density testing as part of the candidate screening process. Following this, a subset of seventeen samples for hydromechanical testing were prepared in accordance with the International Society for Rock Mechanics (ISRM) suggested methods (25). Cylindrical samples of 54 mm diameter parallel to the long-axis of the borehole core samples using a radial drilling machine tool equipped with diamond tipped hollow barrel. The cylinders were then trimmed with a diamond-tipped rock saw so that the length diameter ratio was approximately 2:1; the end surfaces ground to a flatness of < 20 μm using a surface grinding machine tool.

2.3 Testing methodology and experimental protocols

The 39 samples were tested for porosity, density, one sample tested for strength and deformability in uniaxial conditions, seven samples tested for strength and deformability in triaxial conditions, and one sample tested for ultrasonic velocity and permeability in hydrostatic conditions.

2.3.1 Porosity and density

Effective (connected) porosity and density (dry, saturated and particle densities) of all specimens was determined by the ISRM suggested method for porosity/density determination using saturation and buoyancy techniques (25). The specimens were saturated with de-aired and de-ionised water under a vacuum of 6 torr for at least 2 hours before being weighed for porosity and density determination. The dry mass of the specimens was obtained by drying in a fan-assisted oven at 105 to 110°C until they reached a constant mass.

2.3.2 Uniaxial strength and deformation testing

The uniaxial compressive strength and static elastic moduli (Young's modulus and Poisson's ratio) of a single specimen (Table 2) was determined using the ISRM suggested methods for determining the uniaxial compressive strength and deformability of rock materials (25).

The specimen was saturated, as described above for porosity and density determination, and left submerged in de-aired and de-ionised water prior to testing. Upon removal from the water the specimen was immediately wrapped in three layers of cling film, instrumented with direct contact strain gauges, and then tested as soon as practically possible in order to maintain a high degree of saturation (>95%). The specimen was instrumented with two direct contact axial strain gauges (MTS 632.11F-90, accurate to ± 0.01 %) and direct contact circumferential strain gauge (MTS 632.12F-20, accurate to ± 0.01 %). The instrumented specimens were placed within a 4.6 MN capacity servo-controlled hydraulic load frame (MTS 815), between two hardened stainless steel platens. The top platen was spherically seated to prevent eccentric loading and included a 1 MN capacity force transducer (MTS 661.98, accurate to ± 0.34 % of load) to measure the load applied to the sample. A stable contact of approximately 1 kN was made with the specimen to ensure the spherical seated platen was appropriately aligned. The sample was deformed at a constant axial strain rate of 1.0×10^{-5} s^{-1} until macroscopic failure. The axial load, axial load actuator displacement, axial strain and circumferential strain were monitored throughout.

2.3.3 Triaxial strength and deformation testing

The compressive strength and static elastic moduli of 13 samples under different confining pressure conditions were determined using the ISRM suggested methods for determining the strength of rock materials in triaxial compression (25). The specimens were all tested saturated with de-aired and de-ionised water, after being prepared as previously described, but without the application of cling film. Specimens were also re-saturated in the confining pressure vessel to account for drainage during sample preparation.

All specimens tested for strength and deformability in triaxial conditions were placed between two hardened steel platens and then encased in a heat-shrink Polytetrafluoroethylene (PTFE) membrane to prevent ingress of confining fluid into and egress of pore fluid from the specimens. The stainless steel platens used for the saturated specimens were fitted with pore water ports to allow pore pressures within the specimen to be controlled and measured during deformation.

All specimens were instrumented with two axial strain gauges (MTS 632.90F-12, accurate to ± 0.01 %) and one circumferential strain gauge (MTS 632.92H-03, accurate to ±

0.01 %) before being placed within a confining pressure vessel (MTS 656.05). A third platen, not part of the aforementioned specimen assembly, was spherically seated to prevent eccentric loading. This spherically seated platen was in turn fixed to a 2.5 MN capacity force transducer (MTS 661.98B.01, accurate to ± 0.32 % of load) to measure the load applied to the sample.

A stable contact of approximately 1 MPa was made with the specimen to ensure the spherical-seated platen was appropriately aligned. The confining pressure vessel was then closed and filled with mineral oil confining fluid. Confining pressure and pore pressure were then applied simultaneously to 2.0 MPa and 1.0 MPa respectively over a period of 300 seconds. The specimen was considered to be saturated when the pore fluid input line and pore fluid output line showed no differential pressure (as measured by a differential pressure transducer located in the pore pressure intensifier unit). Following saturation, the specimen was left to equilibrate until short-term compaction had ceased, determined to be when no significant further change was observed in axial and circumferential strain (typically a period of a few minutes). Throughout this stage, the confining pressure was maintained at least 0.1 MPa above the pore pressure to ensure that the PTFE jacket did not fail. Specimens were tested with 5 MPa pore-pressure in conventional drained conditions, i.e. with pore fluid lines open and the pore intensifier set to maintain 5 MPa pore-pressure (this was considered appropriate given the porosity of the specimens ranged from 14.1 – 17.5 %). Load was applied to the specimen to achieve a constant axial strain rate of 1.0×10^{-5} s^{-1} until macroscopic failure occurred or a significant amount of post peak-stress axial strain was recorded (between 2 and 5 %). The axial load (differential), axial load actuator displacement, confining pressure, confining pressure actuator displacement, pore pressure, pore pressure actuator displacement, axial strain, circumferential strain and temperature were monitored throughout.

2.3.4 Hydrostatic test with elastic and transport properties

The ultrasonic velocity (P-wave and S-wave), dynamic elastic moduli (Young's modulus, Poisson's ratio, bulk modulus and shear modulus), static bulk modulus and permeability (using pulse decay method) were calculated under various hydrostatic conditions for a single specimen. The specimen was prepared, instrumented, and loaded into the triaxial pressure vessel in the same manner as specimens tested for triaxial strength and deformation testing (see section 2.3.3). A nominal 1 MPa differential stress was maintained throughout the hydrostatic testing to ensure a stable contact was maintained between the specimen and the ultrasonic velocity platens.

Once the specimen was saturated, the confining pressure was increased in 10 MPa steps, at a rate of 0.1 MPa per second, for a total of fourteen stages, with the exception of Stage 1 where the confining pressure was only raised by 8 MPa to reach 10 MPa from the initial pressure conditions. Pore pressure was kept constant at 5 MPa during the test, with the exception of the final stage, where it was decreased to 1 MPa in order to maximise the effective stress applied.

Ultrasonic velocity and permeability measurements were performed at every stage. During each stage, the specimen was allowed first to drain and consolidate, considered to be when no significant further change was observed in axial and circumferential strain (typically a period of a several minutes). Then the ultrasonic velocities were measured along the specimen length using Physical Acoustics Corporation AEwinRock Test for SAMOS software. Three piezoelectric transducers (transponders), housed in the top compression platen, generated P-waves and orthogonally polarised S-waves through the specimen. The P- and S- waves were recorded by three piezoelectric transducers (transceivers) housed in the bottom compression platen. For each sonic velocity test four 5μs pulses, spaced at 500 ms intervals were generated for each wave-type (P, S_1 and S_2). The velocities (V_p and V_s) were then calculated as a mean average of the four readings. Dynamic elastic moduli were calculated as:

$$K = \rho\left(Vp^2 - \frac{4}{3}Vs^2\right) \qquad v = \frac{0.5*\left(\frac{Vp}{Vs}\right)^2 - 1}{\left(\frac{Vp}{Vs}\right)^2 - 1} \qquad E = \frac{9K}{\frac{3K}{\rho Vs^2}+1} \qquad G = \rho Vs^2 \qquad [1]$$

where: K = bulk modulus, ρ = saturated density (bulk density), v = dynamic Poisson's ratio, E = dynamic Young's modulus, and G = dynamic shear modulus (e.g. 26).

Subsequently, permeability was determined using the pulse-decay method. The decay of a 'pulsed' pressure-differential of 1 MPa across the specimen was measured, assuming constant fluid properties, no expansion of fluid lines or reference volumes, and no compressive storage in the specimen. A differential pressure was created across the specimen using a single pore pressure intensifier unit (MTS 286.31) equipped with two isolated reference volumes attached to the top and bottom of the specimen. Permeability was determined as:

$$k = \mu\beta V\left(\frac{\ln\left({\Delta P_i}/{devia\Delta P_f}\right)}{2\Delta t\left({A}/{L}\right)}\right) \qquad [2]$$

Where: k = permeability in m^2, μ = viscosity of pore fluid in Pa.s (for water: 9.55×10^{-4} Pa.s at 20° C), β = compressibility of pore fluid in Pa^{-1} (for water: 5×10^{-10} Pa^{-1} at 20° C), V = reference volume in m^3 (Reference Volume 1 'V_1' = Reference Volume 2 'V_2' = V = 94 cm^3), ${\Delta P_i}/{\Delta P_f}$ = ratio of initial pressure differential to final pressure differential, Δt = the time the pressure decreased from P_i to P_f in s, L = specimen length in m, and A = specimen cross sectional area in m^2**.**

The axial load (differential), axial load actuator displacement, confining pressure, confining pressure actuator displacement, pore pressure, differential pore pressure, pore pressure actuator displacement, axial strain, circumferential strain and temperature were monitored throughout the test.

3 Experimental results

The following sections describe the experimental results. Note that additional details are provided in (27).

3.1 Density and porosity

Figure 3 shows the results obtained for dry density, saturated density, particle density and effective (connected) porosity for 39 test samples. Dry density varied from 2.16 to 2.43 Mg m^{-3}, with an average of 2.28 Mg m^{-3} and standard deviation of 0.06 Mg m^{-3}. Saturated density varied from 2.33 to 2.53 Mg m^{-3} with an average of 2.43 Mg m^{-3} and standard deviation of 0.04 Mg m^{-3}. Particle density varied from 2.62 to 2.71 Mg m^{-3} with an average of 2.68 Mg m^{-3} and standard deviation of 0.02 Mg m^{-3}. The effective porosity of the test samples ranged from 10.3 to 17.5 % with an average of 14.9 % and a standard deviation of 1.7. These ranges reflect the true variability within the lithological succession, as suggested in the description of the Staines No.20 borehole (Table 1).

3.2 Uniaxial compression

Table 2 summarises the result from the uniaxial compression test conducted. A uniaxial compressive strength of 101 MPa was noted with a Young's modulus of 27.4 MPa.

3.3 Triaxial compression

Figure 4 and Table 2 summarise the results from the triaxial compression tests conducted. A progression from brittle to ductile deformation was seen with increasing confining pressure. Examination of the final test samples suggested that the transition occurred at about 60 to 80 MPa confining pressure. All samples showed a peak in stress prior to strain softening; generally this peak stress increased with confining pressure. However, the test conducted at 140 MPa confining stress, had a lower peak stress (303 MPa) than the test at 120 MPa (325 MPa). This may be due to differences in the effective porosity of the test samples, with the stronger test sample having a porosity of 14.8 %, compared with 16.5 %, or due to earlier onset of yield. Post-peak stress behaviour also showed a clear transition from brittle to ductile behaviour: samples tested at lower confining pressures (20 and 40 MPa) underwent Type II brittle failure; samples tested at intermediate confining pressures (60, 80 and 100 MPa) showed (sometimes considerable) post-peak strain softening; samples tested at higher confining pressures (120 and 140 MPa) showed a transition to strain-hardening after an initial phase of post-peak strain softening. Strain results show that increasing confining pressure resulted in greater axial and volumetric strain at peak stress, with the exception of axial strain at 140 MPa, which is slightly lower than that at 120 MPa. The yield stress (see section 4.1) increased with confining pressure up to 60 MPa confining pressure and then decreased with increasing confining pressure.

Generally, Young's modulus increased with confining stress, although there is scatter within this relationship. Poisson's ratio was relatively constant throughout the pressure range with values in between 0.16 and 0.19. At the lowest confining pressure a much higher Poisson's ratio of 0.35 was observed. This however, may be attributed to a high effective porosity of the sample (17.5 %), compared with the other test samples that ranged between 14.1 and 15.4 %.

The Mohr-Coulomb and Hoek-Brown (28; 29) failure envelopes and corresponding failure criterion parameters were calculated for the triaxial and uniaxial compression tests using the peak stress as defined above to represent peak strength. The Mohr-Coulomb approach determines the cohesion (c) and friction angle (Φ) for the rock and was calculated as:

$$\Phi = 2\left(Tan^{-1}\left(\sqrt{B}\right) - 45\right) \qquad C_0 = \frac{UCS}{2Tan(45+\frac{\Phi}{2})} \qquad [3]$$

where B is the slope of the principal stresses plot and UCS is the uniaxial compressive strength, the intercept of the principal stresses plot. The Hoek-Brown approach determines the failure criterion parameters *mb*, *s* and *a*. For intact rock (i.e. when the Geological Strength Index is 100) the *s* and *a* parameters are always 1.0 and 0.5 respectively (see 28). The Hoek-Brown material constant, *mb*, was calculated using RocLab Software, which determines *mb* from the effective principal stresses at failure using a Marquardt-Levenberg fitting technique (30). The Hoek-Brown and Mohr-Coulomb Failure Criterion parameters are presented in Table 3. The Mohr-Coulomb approach determines the cohesion (c) and friction angle (Φ) for the rock. Two results are given, one for the brittle regime (0 to 60 MPa confining stress) and a second for all test results.

3.4 Sonic velocity testing

Figure 5 and Table 4 summarise the ultrasonic velocity measurements on test sample RTL11-121. Figure 5a shows that the relationship between ultrasonic velocity and confining pressure is of similar logarithmic form for both V_p and V_s. The initial discrepancy from the logarithmic trend reflected a change in behaviour from closure of existing micro-cracks in the sandstone at sub 30 MPa, to elastic closure of pores and grains at pressures greater than or equal to 30 MPa. By 100 MPa confining pressure and onward, the rate of change of V_p and V_s tends to a constant V_p of approximately 4390 m s^{-1} and V_s of 2730 m s^{-1}.

The calculated dynamic elastic moduli show a similar logarithmic trend with confining pressure. The dynamic shear modulus (G), bulk modulus (K) and Young's modulus (E) reached an asymptote at around 100 MPa confining pressure. This resulted in average (constant) moduli of 18.2 GPa (G), 22.9 GPa (K) and 43.2 GPa (E). The exception to this behaviour was the dynamic Poisson's ratio, which increased from 0.15 at 10 MPa confining pressure to between 0.18 – 0.2 from pressures greater than or equal to 20 MPa. This observation mirrors that seen for Poisson's ratio measured during triaxial testing (Table 2).

3.5 Hydrostatic permeability

Figure 6 and Table 4 summarise the results from the hydrostatic permeability measurements conducted on sample RTL11-121. The first measurement was taken at a confining pressure of 10 MPa, with an effective stress of 5 MPa, giving a permeability of approximately 3×10^{-16} m^2, or 300 µD. Increasing effective stress to 15 MPa reduced the permeability of the sample to approximately 1×10^{-16} m^2, or 100 µD. Then the permeability remained constant throughout the test up to an effective stress of 125 MPa. During this period, the average permeability calculated was 1.01×10^{-16} m^2, or 102 µD (Figure 6b). A linear best fit shows a slight reduction in permeability with increasing effective stress. However, the spread of permeability results means that there is no clear reduction in permeability and that a constant permeability through the pressure range is a good approximation.

4 Discussion

4.1 Yield envelope

Yield is the onset of permanent, plastic, deformation following purely elastic, recoverable, strain. In rocks that do not show a perfect linear response, as is commonly found, the determination of yield can be somewhat ambiguous. Determining yield is, therefore, not straightforward and more easily determined definitions of strength and failure, such as peak strength (peak stress before failure), have become the commonly reported strength parameter. However, yield is of significance to carbon capture and storage as it represents the stress state at which a permanent change of the reservoir or caprock occurs. Considerable deformation of a reservoir may occur at a stress state greater than the yield condition, but less than peak strength conditions. Wong and co-workers (e.g. 31) showed that sandstones of varying properties have similar yield envelopes when plotted in the differential stress versus effective mean stress space.

Since the onset of yield is not straightforward to determine, several approaches have been developed, including volumetric dilation, monitoring of acoustic emissions (e.g. 31), porosity (e.g. 32), or permeability (e.g. 33). Cuss *et al.* (34) determined yield from stress-strain results by fitting linear regions to the elastic-region and setting a threshold at which a deviation from the linear-elastic response defines yield; this approach was used in the current study.

Yield was estimated for each triaxial compression test and for the uniaxial compression test (Table 2). Yield was considered to be where the stress deviated by more than 1 MPa from the tangent of the elastic region of the stress-strain curve. Error in determining yield was not significant and generally varied by less than 10 % when different sections of the stress-strain curve were considered linear. This was considered a robust method of defining the yield envelope as it eliminated the variability associated with the porosity difference between specimens.

Figure 7 shows the results for yield and peak strength when plotted in the differential (Q) versus effective mean stress (P') space. Differential stress was calculated as the difference between axial (σ_1) and confining stress (σ_3). Effective mean stress was defined as $^1/_3(\sigma_1 + 2\sigma_3) - P_p$, where P_p is pore-pressure. As seen, the peak strength data follow a curved trend with strength continually increasing with mean stress as a power-law. Yield showed a curved form. For tests that displayed shear-localisation (dilatant behaviour), the data fall on the portion of the curve with a positive slope. For tests with pervasive cataclastic flow (contraction), the data fall on the portion of the curve with a negative slope. The apex of the yield envelope signifies the condition of isovolumetric deformation, also referred to as critical state deformation or the brittle-ductile transition.

The post-test observations of failure mode showed that the transition from brittle to ductile deformation occurred between 60 and 80 MPa. Figure 8 shows that at confining pressures less than about 60 MPa, purely brittle deformation was seen with shear localisation (Figure 8a,b). At confining pressures of between 60 and 80 MPa the brittle-ductile transition was seen, with a more distributed series of localised deformation features (Figure 8c). At elevated confining pressures the sample appears to have undergone distributed ductile deformation with the test sample clearly barrelling (Figure 8d). These observations are consistent with those of Wong and co-workers [31]. It should be noted that the brittle-ductile transition at such a pressure represents a depth greater than 2.5 km in the Southern North Sea, which is deeper than the depth of most potential storage sites in the area. Therefore, the SSG tested in the current study is not likely to undergo distributed cataclastic flow (contraction) deformation and that deformation would be brittle (dilatant), or at the brittle-ductile transition (isovolumetric).

Figure 9 shows data from the current study compared with the results presented by Cuss *et al.* (34) and references therein. Wong *et al.* (31) showed that sandstones when normalised by their grain crushing pressure (P^*) have a similar, singular, yield envelope. The grain crushing pressure is the condition where yield occurs under purely hydrostatic conditions and in a *Q-P* plot occurs along the abscissa. This study did not go to sufficient stress to determine the grain crushing pressure, due to limitations in the confining pressure of the apparatus. However, the grain crushing pressure can be determined from the Hertzian contact model (31), which states P^* scales with the grain radius (R) and porosity (ϕ), such that:

$$P^* \propto (\emptyset R)^{-\frac{3}{2}} \qquad [3]$$

Average grain diameter and porosity were determined to be 215 µm and 15 % respectively using scanning electron microscopy. This gave a predicted P^* of 173 MPa, allowing the current study to be normalised and plotted in Figure 9. The current data correspond well with the findings of Wong *et al.* (31) and Cuss *et al.* (34). This is further emphasised in Figure 10 where the current data for SSG are compared with Penrith, Darley Dale and Tennessee Sandstones (from 34). SSG is intermediate in strength between Penrith and Darley Dale Sandstone.

4.1.1 Refinement of the yield envelope

Figure 9 determines the yield envelope from a simple polynomial fit of all available data. Whilst this approach may be considered appropriate, it is not possible to define any parameters of the fit based on physical parameters. The grouped data correspond well with the observed general trend, but when individual rocks are considered, the fit is not perfect. For instance, Boise II plots much higher than the general trend. Furthermore, Berea sandstone displays ductile behaviour at $P/P^* = 0.45$, whereas Sherwood, Penrith and Boise II observe dilatant behaviour. This may derive from difficulty in determining whether deformation is localised or distributed within the transition zone between brittle and ductile deformation. However, it may suggest that a single envelope is not appropriate.

Wong *et al.* (31) observed that most of their normalised data on the ductile side are bracketed by the elliptical cap model (35) given by:

$$\frac{\left(\frac{P}{P^*}-\gamma\right)^2}{(1-\gamma)^2} + \frac{\left(\frac{Q}{P^*}\right)^2}{\delta^2} = 1 \qquad [4]$$

with peaks at (γ, δ) = (0.5, 0.5) and (0.5, 0.7). Therefore, for the ductile side of the yield envelope (from P/P^* = 0.5 to 1.0) the above relationship can be used to estimate yield.

A yield envelope was constructed with the ductile side defined by the DiMaggio & Sandler (35) model with a peak of (0.5, 0.5) and for the dilatant side, a polynomial least-squares best fit was applied through all the data shown in Figure 9.

The form of the yield envelope is further defined by two parameters. The slope of the critical state line (M) defines the position along the abscissa where the peak of the envelope occurs. As shown in Figure 9, the best fit through all the data suggests the peak occurs at P/P^* ~ 0.6, therefore introducing asymmetry to the envelope. As shown by Wong *et al.* (31) the data are generally bound by the δ parameter between 0.5 and 0.7, this defines the height of the yield envelope.

A macro was written in Microsoft Excel to optimise the fit of the recorded data to the yield envelope by adjusting three parameters; P^*, M and δ. This gave the results presented in Figure 10 and Table 5. As seen, the slope of the critical state line varies between 0.77 and 1.25, although for the latter the envelope was fitted to only five data points. For all four sandstone types a good fit is achieved to the data.

4.2 Sherwood Sandstone Group properties

Table 1 and Figure 3 highlight the variability of the SSG in the Staithes No.20 borehole. Test samples were selected to be as similar as practical, so as not to introduce variability into the test results from differences in lithology. As a result there is a general bias in the test data based on the selection of sandstone samples of similar appearance. Even with care, dry density of samples was seen to vary between 2.19 and 2.31 Mg m^{-3} and porosity between 14.1 and 17.5 %. This range in values compares with an overall distribution of dry density of 2.15 to 2.45 Mg m^{-3} and 10 to 18 % porosity for all samples in the Staithes No.20 borehole (Figure 3). The selection of similar samples was successful, although samples RTL11-108 and RTL11-106 had higher porosity than the other test samples. Peak and yield strength (Figure 7) do not suggest that the difference in porosity of these two test samples resulted in anomalous test results. Noy *et al.* (22) report a much broader distribution of porosity for the BSF in the SNS from about 2 to 35 %, with a peak in the distribution of 19 – 21 %. Figure 11**Error! Reference source not found.**a shows the porosity data from Noy *et al.* (22) compared with the current study; it suggests that while the specimens tested are generally close to the average porosity of the BSF, they represents the more tight (low permeability) end of the BSF. However, the test samples reported are representative of the properties of parts of the BSF in the SNS. The SSG from the Staithes No.20 borehole had an average grain diameter of 215 µm. White Rose (36) report an average diameter of between 80 and 200 μm for the BSF, with grain diameters of up to 300 μm recorded. Therefore, based on porosity and grain size, the SSG represents a good analogue for the BSF in the SNS, as shown in Table 6.

At low effective stresses, permeability (Figure 6), ultrasonic velocity (Figure 5a) and the dynamic elastic moduli (Figure 5b) show interesting results. For flow, this represented a greater permeability of a factor of three compared with that seen at higher effective stresses greater than 20 MPa. For the ultrasonic velocity data this was seen as a reduction in the elastic wave velocity. For the dynamic elastic moduli, calculated from the sonic velocity data, this was most apparent in Poisson's ratio, with a reduced value below 25 MPa, which reached a steady value throughout the remaining experiment. This can be explained by the depth of burial of the borehole material used. Samples were taken at depth of between 758.1 to 870.6 m. The average density recorded was 2.62 Mg m^{-3}, which if the borehole is assumed to be a thick sandstone layer would result in a vertical stress of between 16.8 and 19.3 MPa. Assuming a representative density for a sedimentary sequence of 2.2 Mg m^{-3} would result in an *in situ* vertical stress of between 16.3 and 18.8 MPa. Alternatively assuming a vertical stress gradient of 22.5 MPa km^{-1} for the SNS (37; 22) would give an *in situ* stress range of 17.0 to 19.6 MPa. Therefore, the *in situ* vertical stress at the Staithes No.20 borehole is likely to be between 16 and 20 MPa at the depth of the test samples. This range corresponds with the observations described above at low confining pressures. Therefore, the higher permeability and low sonic velocity seen at effective stresses below approximately 20 MPa is most likely the result of closure of pre-existing micro-cracks that resulted from the de-stressing of the borehole core during extraction.

Permeability of sample RTL11-121 was seen to be relatively constant between 15 and 125 MPa effective stress, although a slight reduction in permeability may be inferred. The scatter in the data does not allow an exact relationship to be determined. The reduction of permeability at low pressures followed by a slow reduction, or constant, permeability has been observed previously (e.g. 38). Permeability has, therefore, been assumed to be constant and of the order of 1×10^{-16} m^2, or 0.1 mD. This represents a low sandstone permeability. Generally, permeability values of the order of 40 – 400 mD are reported for the BSF in the SNS (e.g. 22; 39; 20; Table 6). This is 2 to 3 orders of magnitude greater than the permeability observed in the current study. Fontainbleau sandstone has been shown to range in permeability from 0.1 to >1,000 mD (40), although for the porosity range seen in the current study permeability ranges from 300 to 2000 mD. Figure 11b shows the vertical air permeability data reported by Noy *et al.* (22) compared with the current test; note that permeability was measured perpendicular to bedding and therefore vertical permeability is compared, as opposed to the horizontal permeability displayed in Noy *et al.* (22). Figure 11b shows that the permeability of BSF with a porosity of about 15 % varies between 0.02 and 2560 mD, a 5 order of magnitude variation. The Drill String Test (DST) conducted in BSF in the saline aquifer 5/42 in the SNS gave an average permeability of 270 mD (41). Moreover, gas field data in the Hewett Field suggests an average permeability of about 200 mD and even up to 500 mD (42). Therefore, it is clear that while the test samples prepared from the SSG of the Staithes No.20 borehole are representative of those seen in the BSF, they represent the tight end of the permeability spectrum and are not representative of the gas productive zones of the formation likely to be exploited for CCS.

4.3 Reservoir applications

The approach adopted for fitting the yield envelope to the SSG data was seen to be successful. The assumption that all sandstones correspond to a singular normalised yield envelope has previously been shown to be valid (31; 34). Refinement of the envelope using the data published by Wong *et al.* (31) and Cuss *et al.* (34) results in a yield envelope that can be fit to any sandstone yield data as a first approximation. The form of the envelope is dictated by the grain crushing pressure (intercept of the abscissa), the slope of the critical state line and the peak of the critical state. Fitting of this yield envelope to the current data gave a predicted grain-crushing pressure of 171 MPa, which compares well with the prediction from the Herzian contact model of 173 MPa. For Penrith Sandstone the grain crushing pressure was directly measured as 110 MPa. Using the fitting approach, the grain crushing pressure was predicted to be 110 MPa, whereas the Hertzian contact model predicted a grain crushing pressure of 144 MPa.

Figure 12 shows an assessment of the likelihood of permanent deformation of the BSF using reservoir stress/pressure data for five reservoirs and assuming that the BSF has similar yield parameters to the SSG. Parkes *et al.* (17) summarised the available *in situ* data for the Esmond, Gordon, Forbes and Hewitt fields, with additional information in Bentham *et al.* (43) on production history. Differential horizontal stress data is not always reported, therefore the same proportion of differential stress as recorded at Goldeneye (44) was assumed for all fields, consideration was also made of the likely range of differential stresses seen in basins. The stress-path created by depletion was corrected as described in (45) with horizontal stresses reducing by $^{2}/_{3}$ of the pore pressure change. This correction accounts for poroelasticity and includes the Poisson effect and Biot's coefficient. Consideration was also given to a condition whereby the sandstone followed the effective stress-law. However, using the approach described in (45) was more likely to result in deformation and therefore this approach was adopted as a worst case scenario.

As shown in Figure 12 the depletion of the BSF reservoirs of the SNS results in a stress path that remains totally within the elastic region, assuming similar grain size and porosity parameters to the samples of SSG tested. Our analysis highlights that even reducing the formation pressure to zero would still result in stability and would be far from yield. It is expected that re-inflation of the reservoir during CO_2 injection would result in an increase in pore pressure to a magnitude that is less than the starting pore pressure of the field, i.e. if a reservoir is depleted by 10 MPa it will be re-inflated by a maximum of 9 MPa. Figure 12b shows that none of the reservoirs would result in permanent deformation if these limits are adhered to. It can be predicted that increasing pore pressure to a magnitude of 10 MPa greater than the starting pore pressure would still likely to be stable. Figure 12c shows the yield envelope necessary to result in permanent deformation of the reservoir rock. A grain-crushing pressure (P^*) of 31.5 MPa is necessary, this represents a sandstone with extremely high porosity and large grain size. Noy *et al.* (22) report a range of porosity in the BSF in the SNS from 2 to 35 %. Using the Hertzian contact model, the highest porosity would require an average grain size of 290 µm in order to facilitate grain crushing at 31.5 MPa. Boise Sandstone (31) has a predicted P^* of 33 MPa, a measured P^* of 44 MPa, a porosity of 35 % and average grain diameter of 280 µm. Therefore, a sandstone with such a low P^* exist. Such a sandstone does not occur in the SSG described from the Staithes No.20 borehole, but is possible given the porosity range seen in BSF in the SNS. White Rose (36) report grain size up to 300 µm in the BSF of the SNS. However, it should be noted that grain crushing is only likely in the high porosity, large grain-size sections on the BSF in the SNS. The SSG, and by analogy the BSF, appear to be ideal reservoirs for CO_2 sequestration based on mechanical properties, although the SSG tested was seen to have a low permeability. It should be noted that this analysis makes no account of faults that may be present and only assesses the competence of the reservoir rock. Most storage sites in the BSF of the SNS will be faulted (46; 47) and further work is required to assess the implications of fault flow and stability during deflation at extraction and re-inflation during CO_2 injection.

5. Conclusions

This study presents a hydromechanical appraisal of the Bunter Sandstone Formation (BSF) of the Southern North Sea (SNS) by using Sherwood Sandstone Group (SSG) from the Staithes No.20 borehole. A yield envelope for SSG has been produced and demonstrates that it is a very competent sandstone at relevant reservoir depths. Stress analysis of four fields within the SNS suggest that depletion of 10 MPa will not result in permanent deformation of the reservoirs. It also supports that the re-inflation of the fields through the injection of CO_2

will not result in permanent deformation should the injection pressure not exceed the starting reservoir pore pressure. Moreover, increasing the original pore pressure by up to 10 MPa may still result in a stable reservoir rock, although it should be noted this will have other implications such as fault or wellbore stability. However, while the porosity of the SSG in the Staithes No.20 borehole can be seen to represent the lower than average range of the BSF, the recorded permeability was very low (1×10^{-16} m^2; 0.1 mD) and represents the lowest end of the permeability range of the BSF (0.02 to 2500 mD); this would make the storage of CO_2 difficult unless a well-developed fracture network were present. Permeability generally showed little, or no, sensitivity to effective stress. Finally, our results suggest that SSG from the Staithes No.20 borehole suggests that a similar sandstone of the BSF would be a mechanically suitable reservoir rock in the SNS for the sequestration of super-critical CO_2. Further work is required to assess the geomechanical performance of the caprock, as this is also critical to reservoir integrity during depletion of hydrocarbons and reinjection of super-critical CO_2.

Given the paucity of available geomechanical data from depleted hydrocarbon reservoirs (due to commercial confidentiality, historical emphasis on presence of hydrocarbons, permeability, and porosity) and lack of readily available borehole core (due to predominance of open hole drilling, core slabbing, commercial confidentiality, poor curation, and prohibitively cost of offshore drilling to acquire new core), it is difficult to make a reasonable early assessment of reservoir-specific geomechanical performance. Testing of material from an onshore analogue is therefore a cost effective and desirable way to obtain geomechanical parameters to access reservoir viability, and hence to use as an early stage screening tool prior to investing in significantly more costly investigation for design purposes.

Acknowledgements

This paper is the product of research conducted by the British Geological Survey (BGS) as part of the EPSRC CCS Grand Challenge in Geological Storage project CONTAIN (The impaCt of hydrOcarbon depletioN on the Treatment of cAprocks within performance assessment for CO_2 InjectioN schemes; Grant number EP/K036025/1). The authors would like to thank Tony Milodowski for determining porosity and average grain size for the Bunter Sandstone and Jon Harrington and John Williams for help in preparing this manuscript. The BGS authors publish with the permission of the Executive Director, British Geological Survey (NERC).

References

[1] Haszeldine RS. Carbon capture and storage: How green can black be? Science. 2009; 325(5948): 1647–52.

[2] Bickle MJ. Geological carbon storage. Nature Geoscience. 2009; 2: 815–18.

[3] Zoback MD, Gorelick SM. Earthquake triggering and large-scale geologic storage of carbon dioxide. Proc. Natl. Acad. Sci. USA. 2012; 109(26): 10164–68.

[4] DECC. CCS Roadmap: Supporting deployment of Carbon Capture and Storage in the UK. London: Department of Energy and Climate Change; 2012.

[5] Holloway S, Vincent CJ, and Kirk KL. Industrial carbon dioxide emissions and carbon dioxide storage potential in the UK. Keyworth, Nottingham: British Geological Survey, CR/06/185N; 2006.

[6] Arts RJ, Chadwick RA, Eiken O, Thibeau S, Nooner S. Ten years' experience of monitoring CO_2 injection in the Utsira Sand at Sleipner, offshore Norway. First Break. 2008; 26: 65–72.

[7] Van Thienen-Visser K, Breunese JN. Induced seismicity of the Groningen gas field: History and recent developments. The Leading Edge. 2015; 34(6): 664-71.

[8] Zoback, MD, Zinke JC. Production-induced normal faulting in the Valhall and Ekofisk oil fields. In: The Mechanism of Induced Seismicity, CI Trifu, editor. Basel: Birkhäuser; 2002. pp. 403-20.

[9] Verdon JP, Kendall JM, Stork AL, Chadwick RA, White DJ, Bissell RC. Comparison of geomechanical deformation induced by megatonne-scale CO_2 storage at Sleipner, Weyburn, and in Salah. Proceedings of the National Academy of Sciences. 2013; 110(30): E2762-71.

[10] Economides, MJ, Ehlig-Economides CA. Sequestering Carbon Dioxide in a Closed Underground Volume. Journal of Petroleum Science and Engineering. 2010; 70: 123–30.

[11] Wilson M, Monea M. IEA GHG Weyburn CO_2 monitoring & storage project. Summary report 2000-2004. Regina, SK, Canada: Petroleum Technology Research Centre; 2004.

[12] Chadwick RA, Williams GA, Williams JDO, Noy DJ. Measuring pressure performance of a large saline aquifer during industrial-scale CO_2 injection: The Utsira Sand, Norwegian North Sea. International Journal of Greenhouse Gas Control. 2012; 10: 374-88.

[13] Mathieson A, Midgley J, Dodds K, Wright I, Ringrose P, Saoul N. CO_2 sequestration monitoring and verification technologies applied at Krechba, Algeria. The Leading Edge. 2010; 29(2): 216-22.

[14] Bentham M. An assessment of carbon sequestration potential in the UK – Southern North Sea case study. Norwich, UK: Tyndall Centre for Climate Change Research, University of East Anglia, Working Paper 8; 2006.

[15] Bentham M, Mallows T, Lowndes J, Green A. CO2 STORage Evaluation Database (CO_2 Stored). The UK's online storage atlas. Energy Procedia. 2014; 63: 5103-13.

[16] BEIS. 2015 UK Greenhouse Gas Emissions, Final Figures. London: Department for Business, Energy & Industrial Strategy, 2017. 54 pp. https://www.gov.uk/government/collections/final-uk-greenhouse-gas-emissions-national-statistics

[17] Parkes D, Graham CC, Milodowski AE, Harrington JF, Cuss RJ, Ougier-Simonin A, Ambrose K. CONTAIN D2: Identification of candidate geologies and experimental approach. Keyworth, Nottingham: British Geological Survey, OR/15/008; 2015. 90 pp.

[18] Johnson H, Warrington G, Stoker SJ. Permian and Triassic of the Southern North Sea. In: Lithostratigraphic nomenclature of the UK North Sea, R.W.O'B Knox, W.G Cordey, editors. Keyworth, Nottingham: British Geological Survey; 1994.

[19] Brook M, Vincent C, Holloway S. Gestco case study 2a-1: Storage Potential of the Bunter Sandstone in the UK sector of the southern North Sea and the adjacent onshore area of Eastern England. Keyworth, Nottingham; British Geological Survey; CR/03/154, 2003. 37 pp.

[20] Williams, JDO, Jin M, Bentham M, Pickup GE, Hannis SD, Mackay EJ. Modelling carbon dioxide storage within closed structures in the UK Bunter Sandstone Formation. International Journal of Greenhouse Gas Control. 2013; 18: 38-50.

[21] Cameron TDJ, Crosby A, Balson PS, Jeffery DH, Lott GK, Bulat J, Harrison DJ. United Kingdom offshore regional report: the geology of the southern North Sea. London: HMSO for the British Geological Survey; 1992.

[22] Noy DJ, Holloway S, Chadwick RA, Williams JDO, Hannis SA, Lahann RW. Modelling large-scale carbon dioxide injection into the Bunter Sandstone in the UK Southern North Sea. International Journal of Greenhouse Gas Control. 2012; 9: 220-33.

[23] Ketter FJ. The Esmond, Forbes and Gordon Fields, Blocks 43/8a, 43/13a, 43/15a, 43/20a, UK North Sea. In: United Kingdom Oil and Gas Fields, 25 Years Commemorative Volume, IL Abbots, editor. Geological Society, London, Memoirs. 1991; 14: 425-32.

[24] Burley S.D. Patterns of diagenesis in the Sherwood Sandstone Group (Triassic) United Kingdom. Clay Minerals. 1984; 19: 403-40.

[25] Ulusay R, Hudson JA, editors. 2007. The complete ISRM suggested methods for rock characterization, testing and monitoring: 1974-2006. Ankara, Turkey: Commission on Testing Methods, International Society of Rock Mechanics; 2007.

[26] Mavko G, Mukerji T, Dvorkin J. The rock physics handbook: Tools for seismic analysis of porous media. Cambridge: Cambridge University Press; 1998.

[27] Dobbs MR, Kirkham MP, Ougier-Simonin A, Cuss R.J. CONTAIN D3: Experimental parameters from reservoir material testing. Keyworth, Nottingham: British Geological Survey; OR/16/048, 2016. 153 pp.

[28] Hoek E, Carranza-Torres C, Corkum B. Hoek-Brown Failure Criterion – 2002 Edition. In: Proceedings of the. NARMS-TAC Conference. University of Toronto, Toronto; 10 July 2002. pp. 267–73.

[29] Hoek E, Diederichs MS. Empirical estimation of rock mass modulus. Int. J. of Rock Mech. & Min. Sci. 2006; 43: 203–15.

[30] Rocscience Inc. RocLab User's Guide. Toronto: Rocscience Inc; 2007.

[31] Wong T-F, David C, Zhu W. The transition from brittle faulting to cataclastic flow in porous sandstones mechanical deformation. J. Geophys. Res. B. 1997; 102(2): 3009–25.

[32] Baud P, Vajdova V, Wong T-F. Shear-enhanced compaction and strain localization: Inelastic deformation and constitutive modeling of four porous sandstones. Journal of Geophysical Research: Solid Earth. 2006; 111: B12.

[33] Zhu W, Wong T-F. Shear-enhanced compaction in sandstone under nominally dry and water-saturated conditions. Int. J. Rock Mech. Min. Sci. 1997; 34: 372.

[34] Cuss R.J, Rutter EH, Holloway RF. The Application of Critical State Soil Mechanics to the Mechanical Behaviour of Sandstone. Int. J. of Rock Mech. and Min. Sci. 2003; 40: 847-62. DOI: 10.1016/S1365-1609(03)00053-4

[35] DiMaggio FL, Sandler IS. Material model for granular soils. J. Eng. Mech. Div., Am. Soc. Civ. Eng. 1971; 97: 935-50.

[36] Capture Power Limited. White Rose K43: Field Development Report; Technical: Storage. 2016.https://www.gov.uk/government/uploads/system/uploads/attachment_data/file/531187/K43_Field_Development_Report.pdf

[37] Williams JDO, Fellgett MW, Kingdon A, Williamson J.P. *In-situ* stress orientations in the UK Southern North Sea: Regional trends, deviations and detachment of the post-Zechstein stress field. Marine and Petroleum Geology. 2015; 67: 769-784.

[38] Xie S, Jiao C, He S, Xie Q, Gu D, Zhu H, and Sun L. An experimental study on stress-dependent sensitivity of ultra-low permeability sandstone reservoirs. Shiyou Xuebao/Acta Petrolei Sinica. 2011; 32: pp. 489-494.

[39] Heinemann N, Wilkinson M, Pickup GE, Haszeldine RS, Cutler NA. CO_2 storage in the offshore UK Bunter Sandstone Formation. International Journal of Greenhouse Gas Control. 2012; 6: 210-19.

[40] Bourbie T and Zinszner B. Hydraulic and acoustic properties as a function of porosity in Fontainebleau sandstone. *Journal of Geophysical Research: Solid Earth*, 1985; *90*(B13), pp.11524-11532.
[41] Furnival S, Wright S, Dingwall S, Bailey P, Brown A, Morrison D, De Silva R. Subsurface Characterisation of a Saline Aquifer Cited for Commercial Scale CO_2 Disposal. Energy Procedia. 2014; 63: 4926-36.
[42] Cooke-Yarborough P, Smith E. The Hewett Fields: Blocks 48/28a, 48/29, 48/30, 52/4a, 52/5a, UK North Sea: Hewett, Deborah, Big Dotty, Little Dotty, Della, Dawn and Delilah Fields. Geological Society, London, Memoirs. 2003; 20(1): 731-39.
[43] Bentham M, Williams G, Vosper H, Noy D, Williams J, Chadwick A, Kirk K. Using pressure recovery at a depleted gas field to understand saline aquifer connectivity. Energy Procedia. 2017; 114: 2906-20.
[44] Shell. Geomechanics Summary Report. Scottish Power CCS Consortium, UK Carbon Capture and Storage Demonstration Competition Report, UKCCS-KT-S7.19-Shell004. 2011.
[45] Zoback MD. Reservoir geomechanics. Cambridge: Cambridge University Press; 2010.
[46] Williams JDO, Holloway S, Williams GA. Pressure constraints on the CO_2 storage capacity of the saline water-bearing parts of the Bunter Sandstone Formation in the UK Southern North Sea. Petroleum Geoscience. 2014; 20(2): 155-67.
[47] Bentham MS, Green A, Gammer D. The occurrence of faults in the Bunter Sandstone Formation of the UK sector of the Southern North Sea and the potential impact on storage capacity. Energy Procedia. 2013; 37: 5101-09.
[48] Tao G, King MS. Shear-wave velocity and Q anisotropy in rocks: A laboratory study. Int. J. of Rock Mech. and Min. Sci. & Geo. Abs. 1990; 27(5): 353-61).
[49] Erickson KP, Lempp C, Pöllmann H. Geochemical and geomechanical effects of $scCO_2$ and associated impurities on physical and petrophysical properties of Permotriassic Sandstones (Germany): an experimental approach. Environmental Earth Sciences. 2015; 74(6): 4719-43.
[50] Olden P, Pickup G, Jin M, Mackay E, Hamilton S, Somerville J, Todd A. Use of rock mechanics laboratory data in geomechanical modelling to increase confidence in CO_2 geological storage. International Journal of Greenhouse Gas Control. 2012; 11: 304-15.

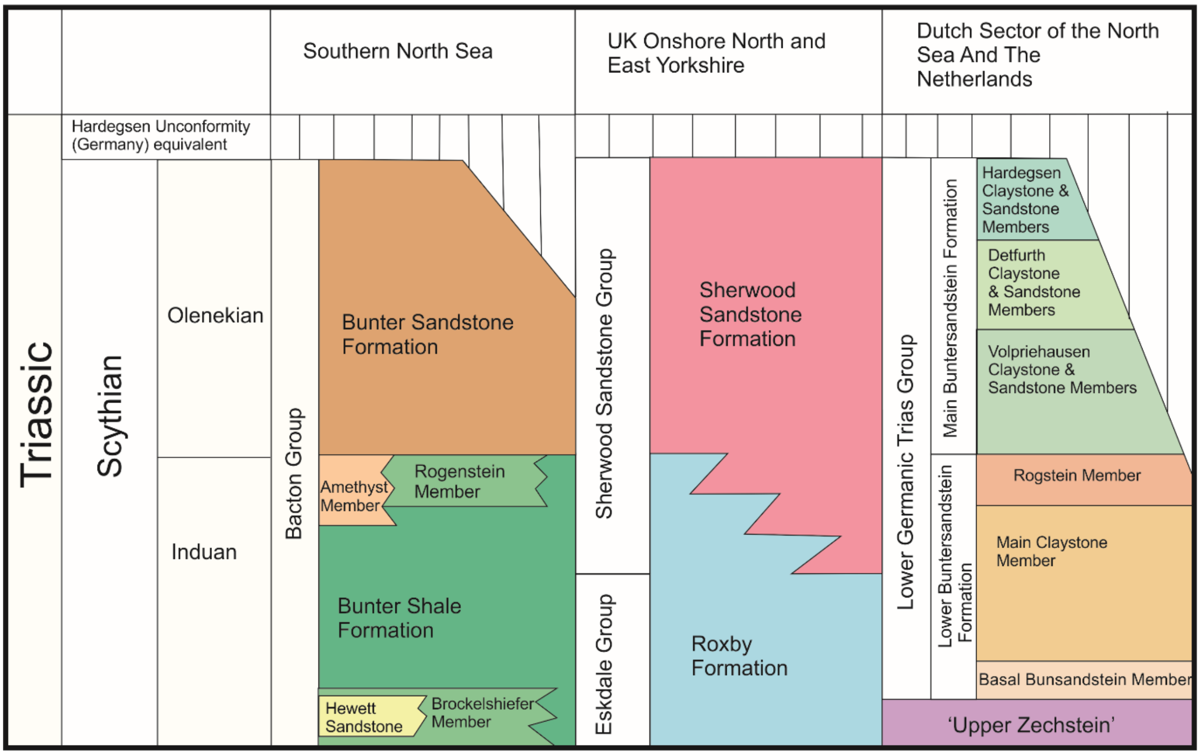

Figure 1 Stratigraphic correlation of the Triassic sediments across the Southern North Sea, onshore UK (North and East Yorkshire) and the Dutch/Netherland sector of the North Sea.

Figure 2 Location of Staithes No. 20 borehole, the extent of Triassic Sandstone (Sherwood Sandstone Group and Bunter Sandstone Formation) onshore and offshore in the UK, and the location of the major gas fields within the Bunter Sandstone Formation.

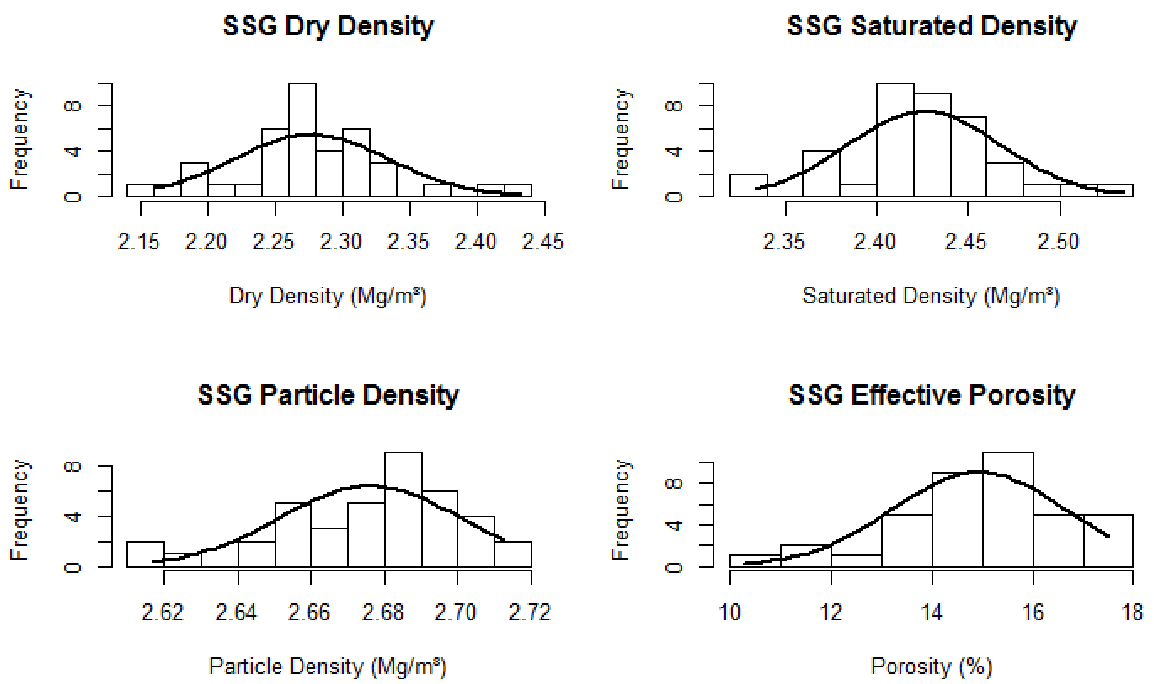

Figure 3 Histogram and density plot for dry density, saturated density, particle density and effective porosity of the Sherwood Sandstone Group from the Staithes No. 20 borehole.

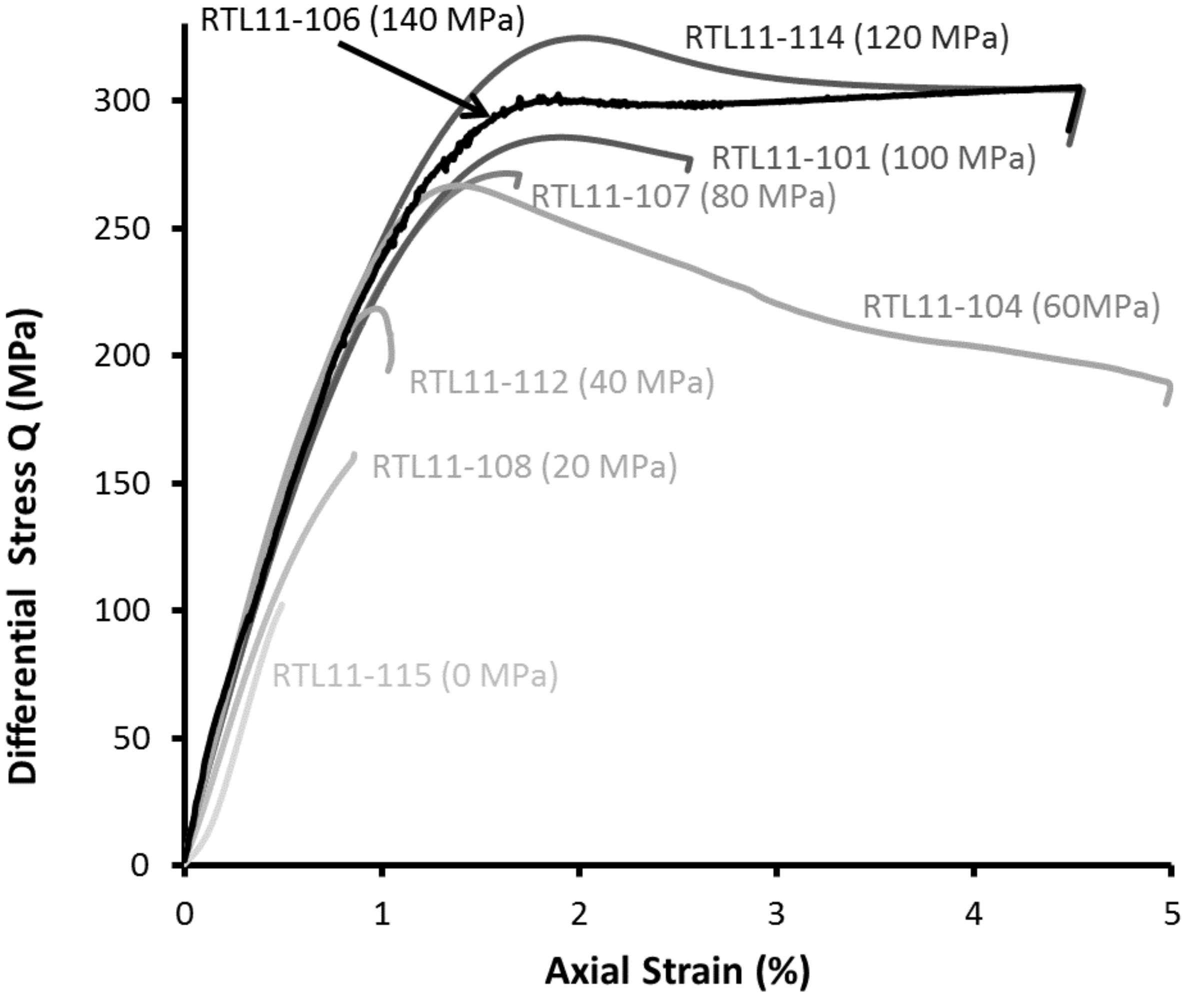

Figure 4 Results for triaxial compression testing of the Sherwood Sandstone Group from the Staithes No.20 borehole showing the transition from brittle to ductile deformation.

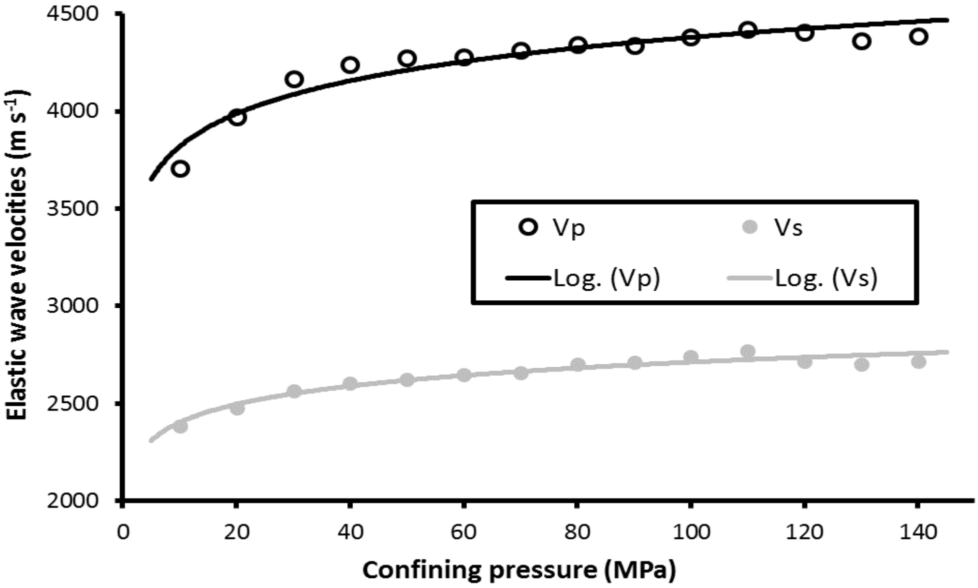

a

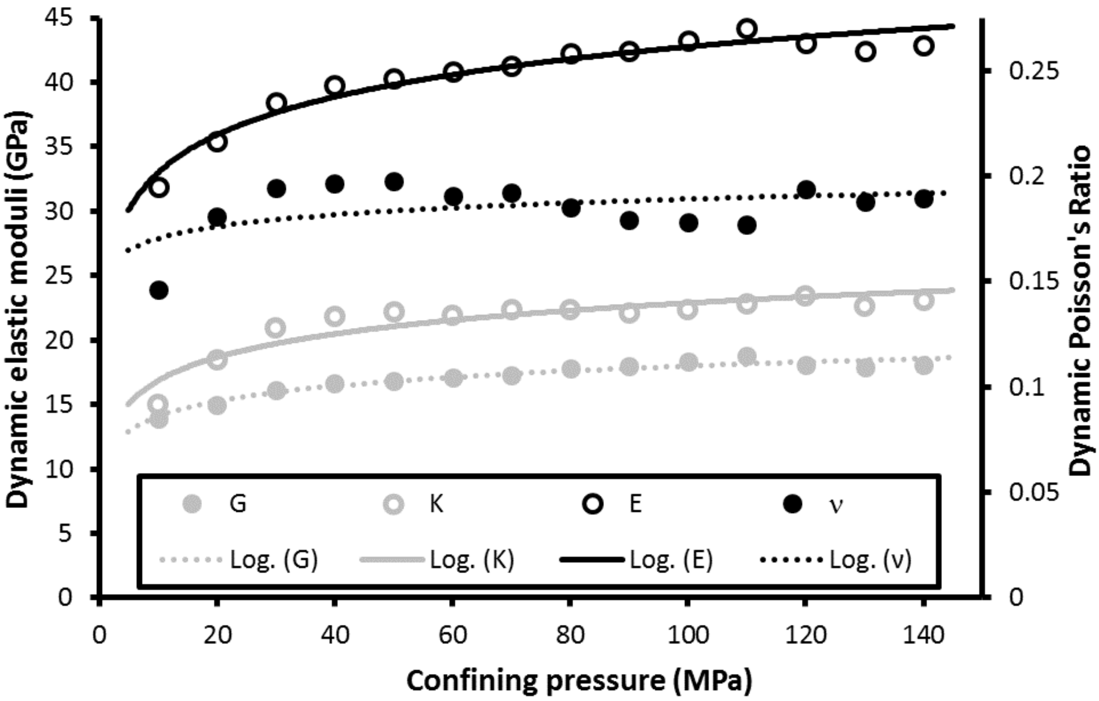

b

Figure 5 Results from ultrasonic velocity testing. a) Ultrasonic velocities; b) dynamic elastic moduli, *E* is Young's modulus, *K* is bulk modulus, *G* is shear modulus and ν is Poisson's ratio.

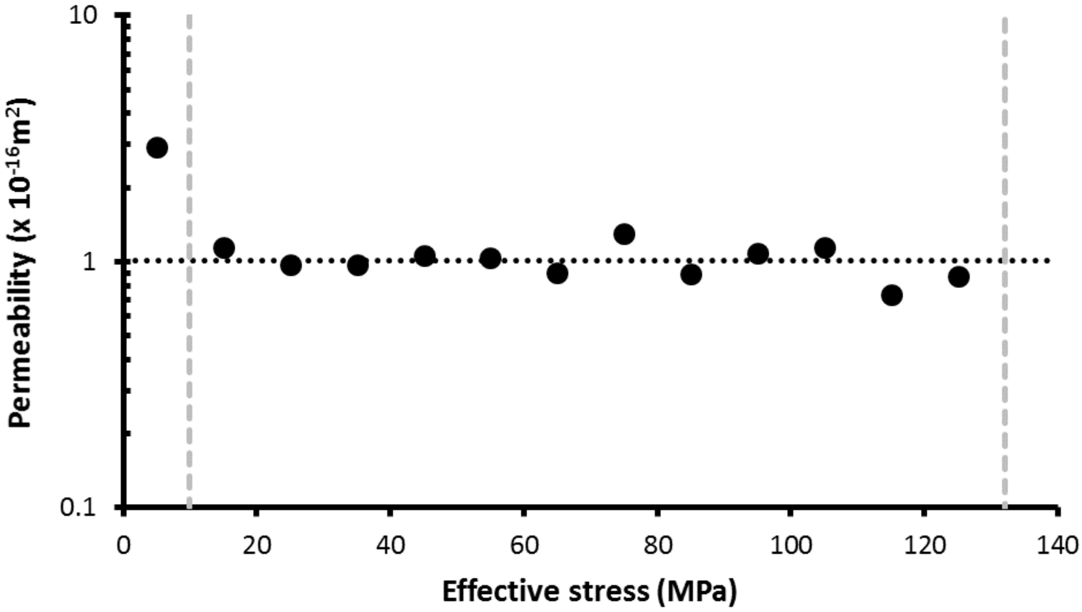

a

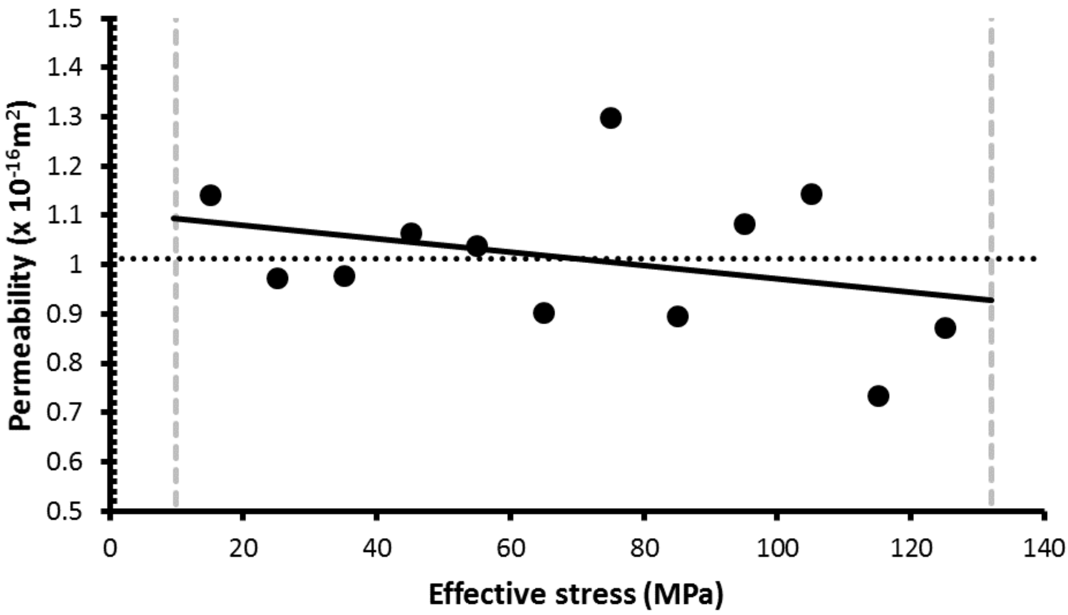

b

Figure 6 Results for hydrostatic permeability testing of sample RTL11-121. a) permeability measurements; b) permeability data between effective stresses of 15 and 125 MPa.

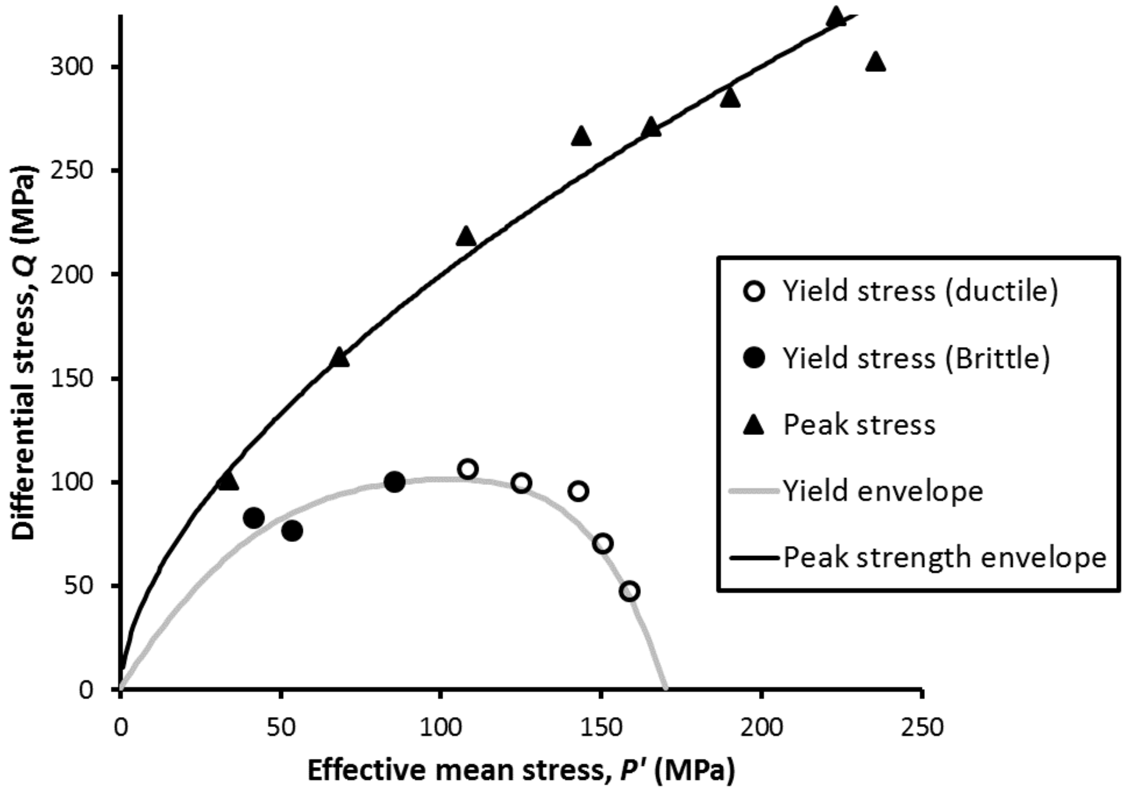

Figure 7 Peak and yield strength in *P´* – *Q* space. Note: open yield stress markers denote deformation on the wet (ductile) side of critical state line and closed markers deformation on the dry (brittle) side.

a) 

b) 

c) 

d) 

e) 

Figure 8 Post-test samples. a) uniaxial compression test; b) brittle deformation at 40 MPa confining pressure; c) brittle-ductile transition at 60 MPa confining pressure; d) ductile deformation at 120 MPa confining pressure; e) ductile deformation with strain hardening and onset of cataclastic flow

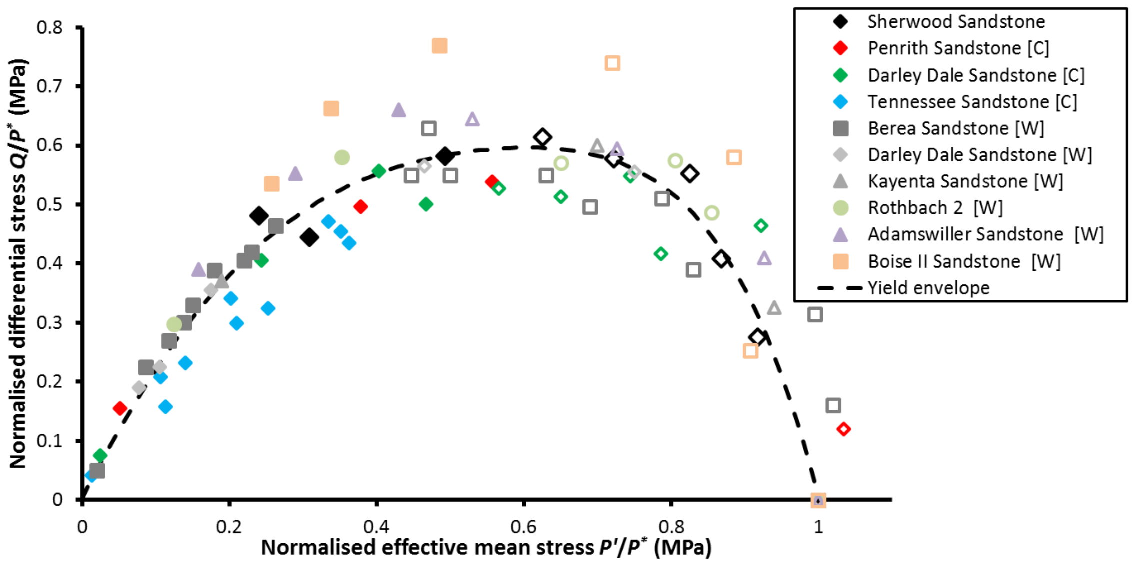

Figure 9 Critical state envelope calculated for 10 sandstone varieties, normalised by the grain crushing pressure (P^*). As seen, all data approximately correspond to a single yield envelope with brittle deformation below $P'/P^* = 0.5$ and ductile deformation above. [C] refers to Cuss *et al.* (33); [W] refers to Wong *et al.* (30); open symbols denote ductile deformation; closed symbols denote brittle deformation.

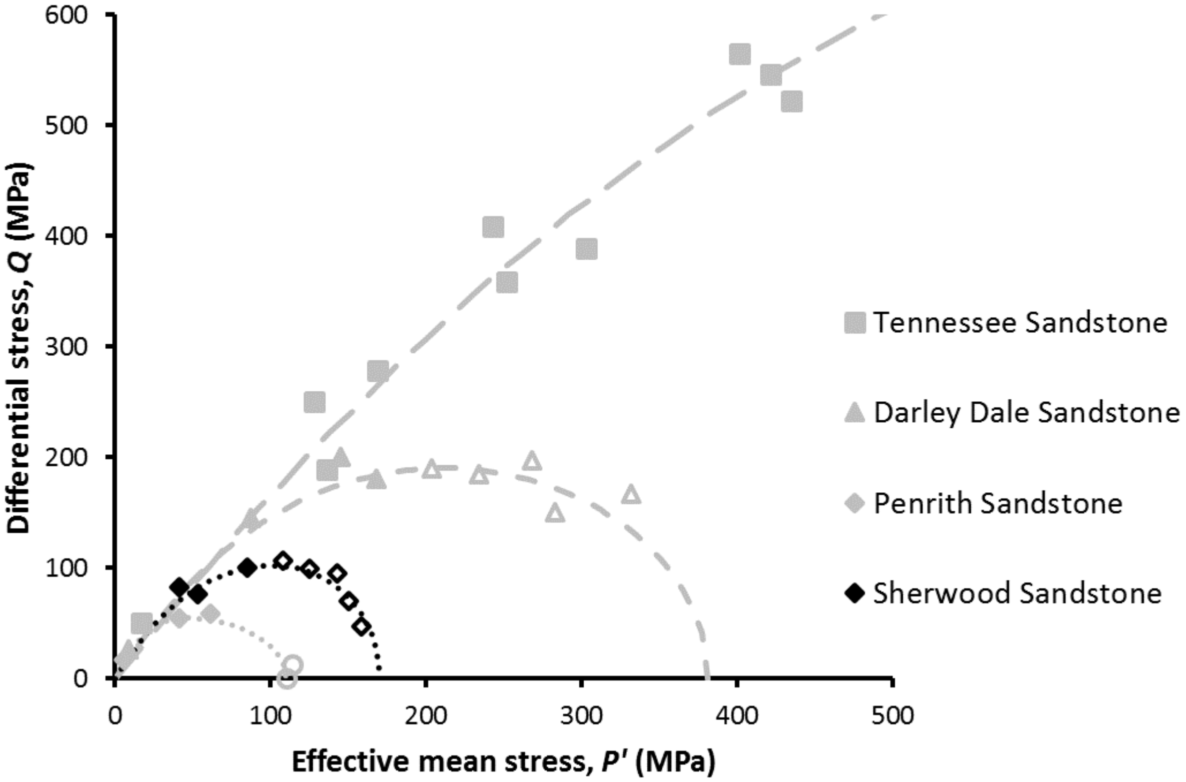

Figure 10 Comparison of the current test data (Sherwood Sandstone Group from the Staithes No.20 borehole) with Penrith, Darley Dale and Tennessee sandstone (from 34). Open symbols denote ductile deformation; closed symbols denote brittle deformation, dashed lines represent the calculated yield envelopes.

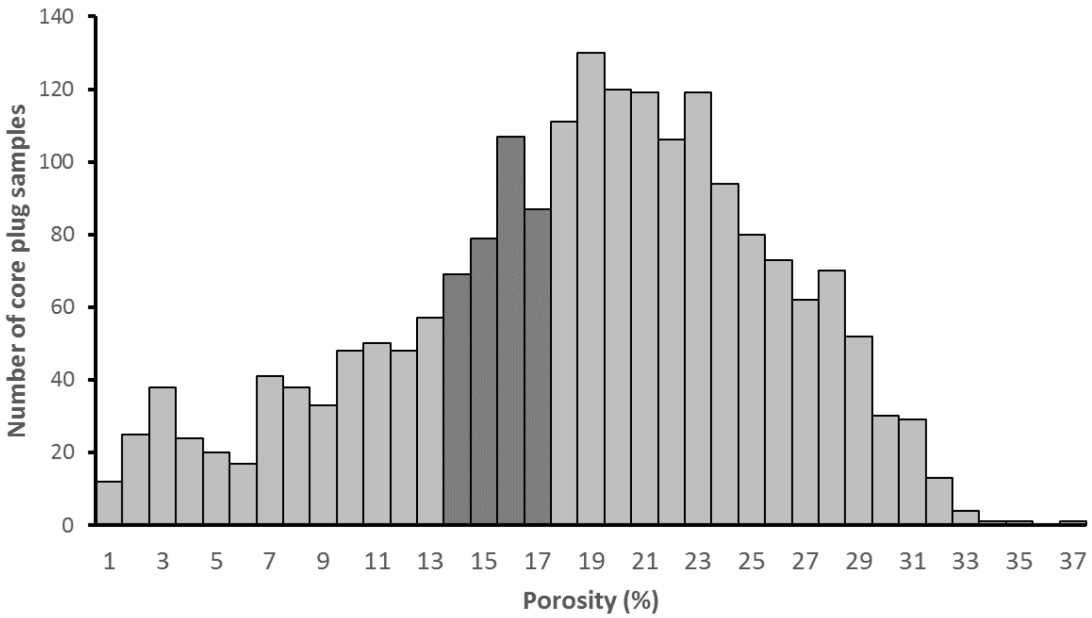

a

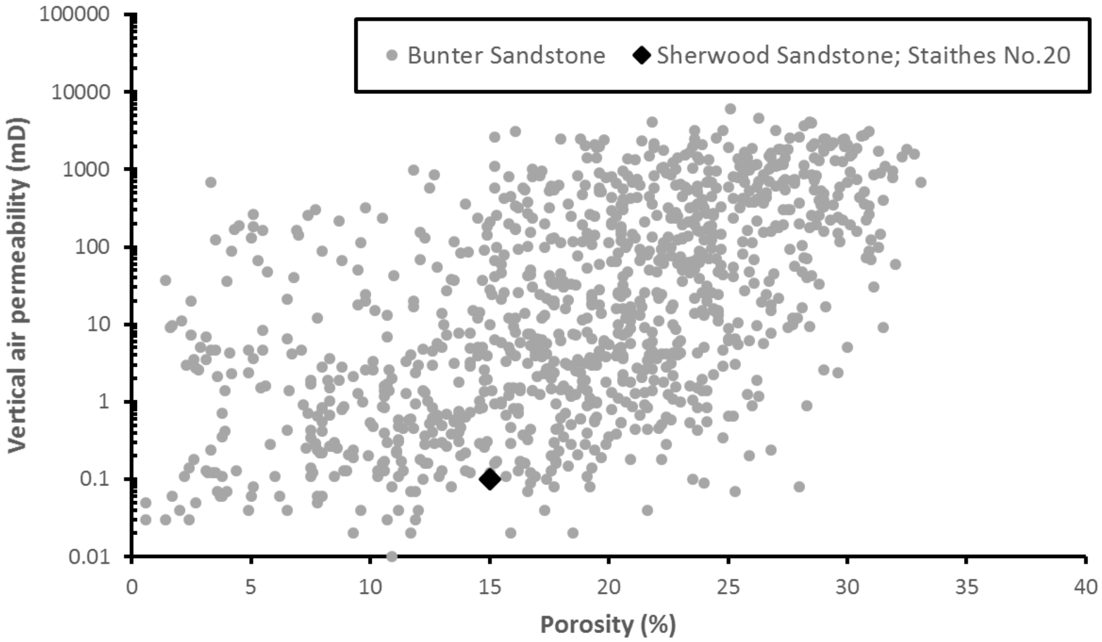

b

Figure 11 Comparing Sherwood Sandstone Group (Staithes No.20) with the Bunter Sandstone Formation: data from (22). a) porosity, note the dark band represents the range of porosity seen in the current study; b) Vertical air permeability versus porosity.

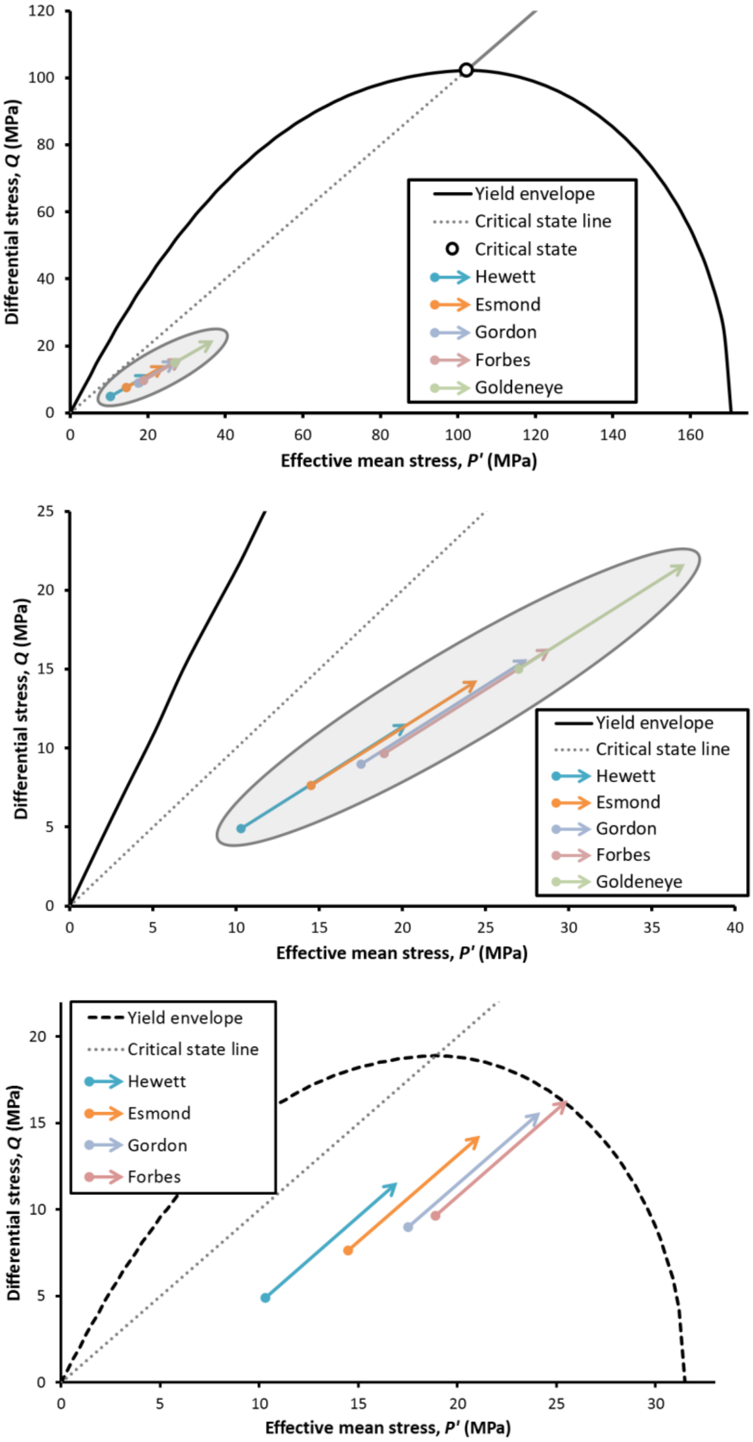

a

b

c

Figure 12 Stress analysis. a) yield envelope with the depletion stress paths for five fields; b) detail of (a); c) yield envelope necessary to result in permanent deformation during drawdown. Note: The grey-shaded ellipse highlights the general stress-space that the reservoirs are located.

Sample Number	Depth Interval (below K.B)	Lithology	Description
RTLII-117	667.5-667.8	*Sandstone*	*Red-brown argillaceous, dolomite and gypsiferous cement, cross-bedded with common mudstone clasts.*
RTLII-119	686.5-686.7	*Sandstone*	*Medium-fine grained, some mudstone bands, micaceous, red-brown, argillaceous, anhydrite cement, parallel laminated.*
RTLII-116	714.3-714.5	*Sandstone*	*Fine-grained, red-brown, cross-laminated, abundant mudstone and siltstone bands.*
RTLII-105	734.5-734.7	*Siltstone*	*Fe and anhydrite cement.*
/	746.8-746.8	*Sandstone*	*Medium-grained, red-brown, argillaceous, Fe and anhydrite cement, muddy lamination.*
RTLII-104	**758.1-758.3**	***Sandstone***	*Red-brown, medium fine grain some siltstone and mudstone bands. Fe calcite cement.*
RTLII-120	757.3-757.4	*Sandstone*	*Fine-grained sandstone, parallel lamination.*
RTLII-107	**763.2-763.4**	***Sandstone***	*Fine-grained, red-brown, micaceous, some clay parting and mudstone flakes, parallel lamination.*
RTLII-118	762.3-762.5	*Sandstone*	
RTLII-101	**771.2-771.4**	***Sandstone***	*Red-brown, medium-grained, rare mudstone partings and mud flakes.*
RTLII-103	778.5-778.8	*Sandstone*	*Medium-fine grain, parallel lamination, red-brown, anhydrite and dolomite cement.*
RTLII-115	**793.5-793.7**	***Siltstone***	*Red-brown*
RTLII-113	795.8-796.1	*Sandstone*	*Red-brown, cross-bedded, medium- fine grained, porous, Fe cement. Some silty calcareous bands.*
RTLII-114	**812.9-813.0**	***Sandstone***	*Medium-fine grained, red-brown, porous, some silty and clay beds. Variable cement - Fe, calcite.*
RTLII-121	**812.6-812.8**	***Sandstone***	
RTLII-108	**823.5-823.6**	***Sandstone***	
RTLII-110	834.4-834.2	*Sandstone*	*Fine, micaceous, red brown, calcareous cement.*
RTLII-102	**846.7-846.9**	***Sandstone***	*Fine-grained, micaceous, red brown, calcareous cement.*
RTLII-112	**862.0-862.2**	***Sandstone***	*Fine grained, red-brown, crossed bedded in part, medium-fine grain, some porous bands and occasional argillaceous bands. Dolomitic cement.*
RTLII-109	862.9-863.1	*Sandstone*	*Red-brown. Fine-grained probable parallel lamination, some mud flakes*

RTLII-106	**870.4-870.6**	***Sandstone***	*Fine grained: porous in the upper part; silty, micaceous, and argillaceous below.*
/	887.5-887.5	*Sandstone*	*Uniform, medium to fine-grained, cross-bedded, red-brown, porous, calcium/gypsum cement, some argillaceous bands and mud flakes.*

Table 1 Sample number, sampling depth, and lithology and borehole description of the samples from the Staithes No.20 borehole.

Sample	Top Depth (m bgl)	Density (Mg m^{-3})			Effective porosity (%)	Confining stress (MPa)	Pore pressure (MPa)	Yield strength (MPa)	Peak strength (MPa)	Yield: Effective mean stress P' (MPa)	Yield: Differential stress Q (MPa)	Young's modulus E (Gpa)	Poisson's ratio *v*	Axial strain at peak stress (%)	Volumetric strain at peak stress (%)	Notes
		Dry	Sat[d]	Particle												
RTL11-115	793.5	2.26	2.41	2.68	15.6	0	0	/	101	/	/	27.4	0.31	0.49	-0.22	Type II Brittle Failure – false peak
RTL11-108	823.5	2.19	2.37	2.65	17.5	20	5	77	160	41	77	24.8	0.35	0.99	0.11	Type II Brittle Failure – false peak
RTL11-112	859.5	2.31	2.46	2.70	14.1	40	5	102	218	69	101	31.1	0.19	1.18	0.76	Type II Brittle Failure
RTL11-104	758.1	2.28	2.42	2.67	14.7	60	5	106	267	90	106	29.6	0.19	1.68	1.01	Unloaded: Brittle/Ductile transition post-peak
RTL11-107	763.2	2.27	2.43	2.69	15.4	80	5	100	272	108	100	27.2	0.18	2.0	1.53	Unloaded: Ductile post-peak
RTL11-101	771.2	2.28	2.43	2.69	15.1	100	5	96	286	127	96	26.9	0.17	2.31	1.83	Unloaded: Ductile post-peak
RTL11-114	812.9	2.29	2.43	2.68	14.8	120	5	71	325	139	71	30.1	0.16	2.48	2.22	Unloaded: Ductile/Strain Hardening transition post-peak
RTL11-106	870.4	2.22	2.39	2.66	16.5	140	5	48	303	151	48	37.0	0.19	2.36	2.47	Unloaded: Strain Hardening

Table 2 Results from the uniaxial and triaxial compressive tests on the Sherwood Sandstone Group from the Staithes No.20 borehole.

Stages used for calculation	**Mohr-Coulomb Manual Calculation**			**Mohr-Coulomb RocLab Calculation**			**Hoek-Brown RocLab Calculation**			
	c	**ϕ**	**UCS**	**c**	**ϕ**	**UCS**	**mb**	**s**	**a**	**UCS**
All Stages	35	28.4	117	38.0	27.6	120.2	6.2	1.0	0.5	120
0, 20, 40, 60 MPa	26.0	37.0	104	25.0	37.9	100	10.9	1.0	0.5	100

Table 3 Strength parameters: Mohr-Coulomb and Hoek-Brown failure criteria parameters. Where c is cohesion, ϕ is the friction angle, UCS is the uniaxial compressive strength, and mb, s, and a are the Hoek-Brown parameters.

Confining pressure (MPa)	Effective stress (MPa)	Average V_p (ms^{-1})	Average V_{s1} (ms^{-1})	Average V_{s2} (ms^{-1})	Average V_{sav} (ms^{-1})	Dynamic Shear Modulus G (GPa)	Dynamic Bulk Modulus K (GPa)	Dynamic Young's Modulus E (GPa)	Dynamic Poisson's Ratio v	Permeability k (m^2)
10	5	3706	2456	2314	2385	13.9	15.0	31.9	0.15	2.92×10^{-16}
20	15	3969	2562	2393	2478	15.0	18.5	35.5	0.18	1.14×10^{-16}
30	25	4166	2612	2521	2567	16.1	21.0	38.5	0.19	9.74×10^{-17}
40	35	4241	2653	2560	2606	16.6	21.8	39.8	0.20	9.78×10^{-17}
50	45	4274	2658	2590	2624	16.8	22.2	40.3	0.20	1.07×10^{-16}
60	55	4280	2672	2621	2647	17.1	22.0	40.8	0.19	1.04×10^{-16}
70	65	4311	2692	2628	2660	17.3	22.4	41.3	0.19	9.03×10^{-17}
80	75	4344	2736	2663	2700	17.8	22.4	42.3	0.19	1.30×10^{-16}
90	85	4339	2782	2642	2712	18.0	22.1	42.4	0.18	8.96×10^{-17}
100	95	4379	2808	2672	2740	18.4	22.4	43.3	0.18	1.08×10^{-16}
110	105	4422	2816	2724	2770	18.8	22.8	44.2	0.18	1.15×10^{-16}
120	115	4407	2754	2678	2716	18.0	23.5	43.1	0.19	7.34×10^{-17}
130	125	4359	2745	2660	2703	17.9	22.7	42.4	0.19	8.73×10^{-17}
140	135	4387	2752	2678	2715	18.0	23.0	42.9	0.19	/

Table 4 Results from the sonic velocity study and hydrostatic permeability testing of sample RTL11-121 during triaxial compressive testing [812.6m depth; dry density = 2.31 Mg m^{-3}; saturated density = 2.45 Mg m^{-3}; particle density = 2.68 Mg m^{-3}; effective porosity = 14.1 %]

.

Sandstone	**Study**	***M***	***δ***	***P^** fit (MPa)**	***P^** predicted (MPa)**	***P^** measured (MPa)**
Sherwood	1	1	0.6	171	173	
Penrith	2	1.25	0.5	110	144	110
Darley Dale	2	0.91	0.5	381	285	
Tennessee	2	0.77	0.5	1540	2370	

Table 5 Critical state parameters for four sandstone varieties.

	Formation	Permeability (mD)	Porosity (%)	Grain size (µm)	UCS (MPa)	E (MPa)	V_p (km s^{-1})	V_s (km s^{-1})
Current	SSG	0.1-0.3	10-18	215	101	24.7-37	3.7-4.4	2.3-2.8
White Rose (35)	BSF	0.03-10,000	6-34	75-200	45	13-22	1-3.4	
Noy et al. (22)	BSF	0.01-10,000	2-35					
Tao & King (48)	BSF		17	<200			3.2	1.9
Erickson et al (49)	BSF	0.005-1			36			
Olden et al (50)	BSF	1-3,500	9-30	medium		8-22		

Table 6 Comparison of current test data for the Sherwood Sandstone Group with reported values for the Bunter Sandstone Formation.